



**CHALMERS**  
UNIVERSITY OF TECHNOLOGY

## **Predicting orientation in extruded wood polymer composites**

Downloaded from: <https://research.chalmers.se>, 2024-09-27 10:17 UTC

Citation for the original published paper (version of record):





Pashazadehgaznagh, S., Suresh, A., Ghai, V. et al (2024). Predicting orientation in extruded wood polymer composites. *Physics of Fluids*, 36(9). <http://dx.doi.org/10.1063/5.0224011>

N.B. When citing this work, cite the original published paper.

RESEARCH ARTICLE | SEPTEMBER 11 2024

## Predicting orientation in extruded wood polymer composites

Special Collection: [John Michael Dealy \(1937-2024\): Celebrating His Life](#)

Sajjad Pashazadeh ; Arvinth Seshadri Suresh ; Viney Ghai ; Tobias Moberg; Anders Brolin ; Roland Kádár 



*Physics of Fluids* 36, 093109 (2024)

<https://doi.org/10.1063/5.0224011>



### Articles You May Be Interested In

Studies on single-screw extrusion of wood-polymer composites with yield stress and slip effects

*AIP Conf. Proc.* (January 2020)

The effect of extrusion speed on mechanical properties of starch-based biocomposite

*AIP Conf. Proc.* (April 2020)

The effects of electron beam irradiation on LLDPE/CY biocomposites: Tensile and morphology properties

*AIP Conf. Proc.* (March 2020)

## AIP Advances

### Why Publish With Us?

 <b>19 DAYS</b> average time to 1st decision	 <b>500+ VIEWS</b> per article (average)	 <b>INCLUSIVE</b> scope
--	--	---

[Learn More](#)



# Predicting orientation in extruded wood polymer composites

Cite as: Phys. Fluids **36**, 093109 (2024); doi: [10.1063/5.0224011](https://doi.org/10.1063/5.0224011)

Submitted: 18 June 2024 · Accepted: 13 August 2024 ·

Published Online: 11 September 2024



View Online



Export Citation



CrossMark

Sajjad Pashazadeh,<sup>1,a)</sup> Arvinth Seshadri Suresh,<sup>1</sup> Viney Chai,<sup>1</sup> Tobias Moberg,<sup>2</sup> Anders Brolin,<sup>3</sup> and Roland Kádár<sup>1,4,5,a)</sup>

## AFFILIATIONS

<sup>1</sup>Department of Industrial and Materials Science, Chalmers University of Technology, Gothenburg SE 412 96, Sweden

<sup>2</sup>Stora Enso AB, Circular Solutions, Packaging Solutions, Hyltebruk SE 314 81, Sweden

<sup>3</sup>Stora Enso AB, Group Innovation and R&D, Karlstad Research Centre, Karlstad SE 650 09, Sweden

<sup>4</sup>FibRe-Centre for Lignocellulose-based Thermoplastics, Department of Chemistry and Chemical Engineering, Chalmers University of Technology, Gothenburg SE 412 96, Sweden

<sup>5</sup>Wallenberg Wood Science Centre, Chalmers University of Technology, Gothenburg SE 412 96, Sweden

**Note:** This paper is part of the special topic, John Michael Dealy (1937-2024): Celebrating His Life.

<sup>a)</sup>Authors to whom correspondence should be addressed: [sajjadp@chalmers.se](mailto:sajjadp@chalmers.se) and [roland.kadar@chalmers.se](mailto:roland.kadar@chalmers.se)

## ABSTRACT

A general procedure for combining material functions and numerical modeling to predict the orientation of highly filled wood polymer composites (WPCs) in a single screw extrusion and validation thereof is elaborated in this study. Capillary rheometry was used to determine the shear viscosity and wall slip functions as well as the melt density of the biocomposites. The numerical model consisted of a model film die where the melt flow was simulated using a finite element method in the generalized Newtonian constitute equation framework. Fiber orientation was modeled using the Folgar–Tucker approach and included fiber–fiber interaction during the process. Reference extrusion tests were performed on a single screw extruder on the biocomposites. The extrusion setup included two melt pressure transducers that were used to determine the die inlet initial conditions (end of the extruder/die inlet) and provide feedback on the wall slip boundary conditions (pressure discharge along the die). Overall, the pressure error between experiments and simulations was less than 6.5% for all screw speeds investigated in 20 wt. % WPCs. Extrudates were produced, and the wood fiber orientation was estimated based on scanning electron microscopy micrographs and image analysis and compared with the simulations of fiber orientation. We show that the general procedure outlined can be calibrated to predict the overall orientation distribution of wood fiber biocomposites during single screw extrusion.

© 2024 Author(s). All article content, except where otherwise noted, is licensed under a Creative Commons Attribution-NonCommercial-NoDerivs 4.0 International (CC BY-NC-ND) license (<https://creativecommons.org/licenses/by-nc-nd/4.0/>). <https://doi.org/10.1063/5.0224011>

## I. INTRODUCTION

Wood polymer composites (WPCs), and, in particular, highly filled compositions thereof, are becoming a viable commercial alternative to conventional plastics due to their renewable content along with their comparatively good mechanical characteristics.<sup>1–4</sup> However, from a processing perspective, using WPCs, especially highly filled with high aspect ratio fibers, can be problematic. Complex flow-induced de-agglomeration-agglomeration dynamics, surface instabilities, and thermal degradation require a fundamental understanding of WPC processing flows.<sup>5–7</sup> This, together with the often inability of current conventional plastics-based processing technology to facilitate highly filled WPC throughput, results in the need to redesign processing components tailored for the new material compositions. In this

context, modeling of extrusion and experimental validation thereof is of paramount importance.

Modeling the flow dynamics of WPCs in extrusion can be challenging due to the interplay between complex flow configurations and rheologically complex fluids. These challenges can include multiphase flows, fiber orientation dynamics, intensive fiber–fiber interactions, viscoelastic and thermal dissipation effects, etc. In this context, melt rheological measurements are an essential requirement to obtain the necessary parameters for simulations. Several studies have been dedicated to the rheological characterization of WPCs,<sup>8–15</sup> through which essential material properties such as shear viscosity functions, viscoelastic/plastic parameters of constitutive models, and slip velocity/length can be obtained. Selecting an appropriate constitutive model

can be vital in obtaining realistic predictions of melt flows.<sup>16–19</sup> Furthermore, connecting numerical modeling directly with experimentally determined inputs as well as a validation reference is one of the key aspects for rigorous modeling of wood fiber biocomposite processing.

In general, modeling of single-screw extrusion can be categorized into four zones: feeding zone (solid transport), compression/melting, metering/die(melt flow), and die flow zone.<sup>16</sup> Wilczyński *et al.*<sup>20</sup> have developed a global model for single screw extrusion of wood flour composites, which consists of individual models for all four aforementioned zones. This model is able to predict pressure and temperature profiles, extrusion output, melting profile, and power consumption. Thus, the authors performed a brief study on the influence of material on the extruder operation. Their estimated pressure was higher than the experimental pressure since slip effects were ignored in their model. Furthermore, a more detailed study was performed by the same authors,<sup>21,22</sup> focusing on the modeling of WPCs in the metering and die zones by taking wall slip into account. Wall slip effects were simulated using the commercial code Polyflow (Ansys, Inc., Canonsburg, PA, USA) by applying Navier slip condition in the screw metering zone and a conical die at three different screw speeds of 20, 50, and 80 rpm; according to their study, implementing the slip effect causes a reduction of computed pressure, and consequently, better validation with experimental pressure data.<sup>21</sup> Liese and Wünsch<sup>23</sup> modeled the flow of WPCs within extrusion dies numerically to investigate the reason behind the significant pressure drop occurring between the die inlet and parallel zones (where the flow is split into two parallel sub-flows); see Ref. 24. It was observed that in regions of high strain, the viscosity increased by  $10^5$  Pa s because of a combination of shear thinning and strain thickening behavior, which ultimately led to the high pressure drop.

The orientation of fibers plays a crucial role in the properties of the processed material. Its importance is witnessed in both the manufacturing phase, when the composite is in the molten state, and in the post-processing phase, when it solidifies. Hence, it is vital to investigate the fiber orientation state in composites. Short fiber composites such as WPCs are considered to be a concentrated suspension.<sup>25</sup> Orientation of fibers in a dilute suspension where fiber–fiber interaction is negligible can be modeled based on the Jeffery model.<sup>26</sup> However, in a concentrated suspension, the interaction between fibers is prevalent.<sup>27</sup> This necessitates the use of a much more sophisticated model that includes the fiber–fiber interaction and for that reason, the Folgar–Tucker model<sup>27</sup> (F–T model) was chosen in the current study.

The main goal of the present study is to predict fiber orientation in highly filled wood fiber composites melt flow through elaborating all the characterization and reference experimental data required to rigorously validate the results in single-screw extrusion. Thus, this study extends from the coupling of the Folgar–Tucker model to the flow and constitutive relations, capillary rheometry to determine the steady shear viscosity functions and slip behavior, experimental data analysis in the form of *in situ* melt pressure and *ex situ* inline image analysis, and finally to scanning electron microscopy (SEM) image analysis of fiber orientation, where the flow chart in Fig. 1 exhibits the procedure graphically. Such a broad approach is challenging but necessary for predicting and optimizing highly filled WPCs processing. The work thus extends the current understanding of WPC flows by including for the first time the orientation dynamics of wood fibers and fiber–fiber interaction in extrusion with a film die.

## II. EXPERIMENTAL METHODS AND MATERIALS

### A. Materials

Polypropylene (PP) based wood fiber composites were supplied by Stora Enso (Helsinki, Finland) in the form of pellets, comprising 5, 20, and 40 wt. % wood fiber content, in addition to the unfilled PP. Pellets were dried under a strict protocol to minimize the possibility of bubble formation during the extrusion process.<sup>7</sup> Pellets were kept in a convection oven (Memmert, UF260plus, Germany) at 90 °C for five days prior to processing. Measuring the size and aspect ratio of fibers was a challenge in our study due to the wide range of fiber sizes. We used scanning electron microscopy (SEM) on pure fibers (see Fig. SI2) and then calculated the average length and diameter. Our analysis shows that the average length of the fibers is around 150  $\mu\text{m}$  and the diameter is  $\sim 28$   $\mu\text{m}$ . For more details on fiber size, see Fig. SI3. The thermal properties of the investigated WPCs from thermogravimetric analysis and differential scanning calorimetry can be found in Ref. 7.

### 1. Capillary rheometry

Rheological characterization is essential for providing material and flow input parameters into computational fluid dynamics (CFD) simulations, such as viscosity functions and slip velocity as a function of shear rate. The rheological characterization of the WPCs were done at  $T = 180$  °C using a Göttfert RG 20 (Buchen, Germany) capillary rheometer. The Bagley correction<sup>28</sup> was applied to correct the wall shear stress  $\sigma_w$  due to contraction flow errors when pressure is induced at the entrance to the capillary die. Two round shape dies having the same radius  $R = 0.5$  mm, and different aspect ratios,  $L/R = 20/0.5 = 40$ , and  $L/R = 0/0.5 = 0$  were used to implement the Bagley correction. The Weissenberg–Rabinowitsch<sup>29</sup> correction was implemented to correct for the assumed parabolic velocity profile to obtain the (true) shear rate  $\dot{\gamma}$ . The Mooney method<sup>30</sup> was applied to determine the slip velocity and slip length. Thus, for a round die of diameter  $D$  and considering the power-law model

$$\eta(\dot{\gamma}_a) = K\dot{\gamma}_a^{n-1}, \quad (1)$$

subsequently, the slip velocity  $V_s$  can be determined as<sup>31</sup>

$$V_s = \frac{D}{8} \left[ \dot{\gamma}_a - \frac{4n}{3n+1} \left( \frac{\sigma_w}{K} \right)^{n-1} \right], \quad (2)$$

where  $K$  and  $n$  are the consistency and flow indices, respectively, and  $\sigma_w$  is the (corrected) wall shear stress. Consequently, the slip length ( $b$ )<sup>32</sup> can be obtained by assuming a linear relationship between slip velocity  $V_s$ , and no-slip wall shear rate ( $\dot{\gamma}_{ns} = \dot{\gamma}_a - \dot{\gamma}_{slip}$ ) as follows:

$$V_s = b \cdot \dot{\gamma}_{ns}. \quad (3)$$

The Weissenberg–Rabinowitsch correction can be applied for  $\dot{\gamma}_{ns}$ . In this study, in order to see the effects of the slip lengths, on the pressure of the simulations, two scenarios of wall boundary conditions were taken into account:

- (i) In the first scenario, we assume  $b = \max\{b(\dot{\gamma})\}$  for each concentration.
- (ii) In the second scenario, we assume the slip length is a function of shear rate, using the following relation:

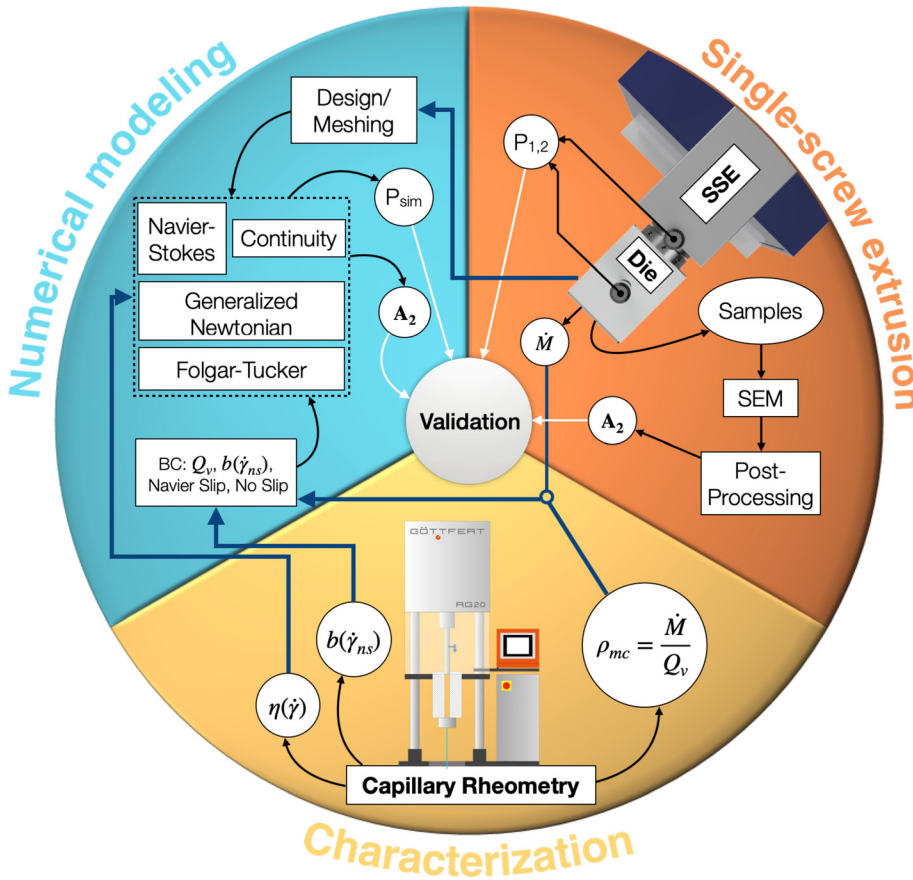


FIG. 1. Flow chart, which represents the interplay between processing, modeling, and characterization for predicting orientation in wood fiber biocomposites.

$$b(\dot{\gamma}_{ns}) = b_{max} - \frac{b_{max} - b_{min}}{1 + \frac{|\dot{\gamma}_{ns}|}{\dot{\gamma}_c}}, \quad (4)$$

where  $b_{max}$  and  $b_{min}$  are maximum and minimum limits of the slip length and  $\dot{\gamma}_c$  is the critical shear rate where the transition between limits occurs, see Ref. 33 for further details.

## 2. Determination of melt density

The melt density of all compositions was determined by capillary rheometry at 180 °C (die temperature) using a round die with  $L/R = 20/0.5 = 40$ , at a shear rate of 200 1/s. Melt densities were obtained through the ratio of the mass flow rate over the volumetric flow rate as follows:

$$\rho_{mc} = \frac{\dot{M}}{Q_v}, \quad (5)$$

where  $\rho_{mc}$ ,  $\dot{M}$ , and  $Q_v$  are density in the melt state, mass flow rate, and volumetric flow rate, respectively. For each concentration, the density measurements were carried out in triplicate, and the average was taken. Applying the composite rule of mixtures yields

$$\rho_{mc} = \rho_f \phi_{vol} + \rho_{mp}(1 - \phi_{vol}), \quad (6)$$

where  $\rho_{mc}$ ,  $\rho_f$  and  $\rho_{mp}$  are the melt densities of the biocomposite, fibers, and the polymer matrix, respectively.

## B. Single screw extrusion

Materials were extruded using a 19/25D (barrel diameter of  $D_b = 19$  mm, barrel length =  $25 \times D_b$ ) single screw extruder (Brabender GmbH, Duisburg-Essen, Germany) with a compression screw (ratio of 2/1). A schematic of the experimental setup, including the single-screw extruder, melt pressure data acquisition system, and imaging setup, is shown in Fig. 2. A standard film die (see Fig. SI1) was mounted to the extruder with contraction in the  $y$ -direction, and bi-axial expansion characteristics in the  $x$  and  $z$  (flow) directions. The temperatures of the heating elements from the feeding zone toward the die were set to 150, 170, 180, and 180 °C, respectively. WPCs were extruded at three different screw speeds ( $n$ ) of 21, 66, and 121 rpm. The pressure was measured using two Terwin 2000 series transducers (Terwin Instruments Ltd., Bottesford, UK). The first transducer was placed at the end of the extruder/die entrance, and the 2nd transducer was positioned at 80 mm from the die inlet, Fig. 2.

## C. Determining the inlet velocity

### 1. Mass flow rate

The average velocity, or volumetric flow rate, is a crucial variable as inlet boundary condition in fluid flow simulations, while in processing, the

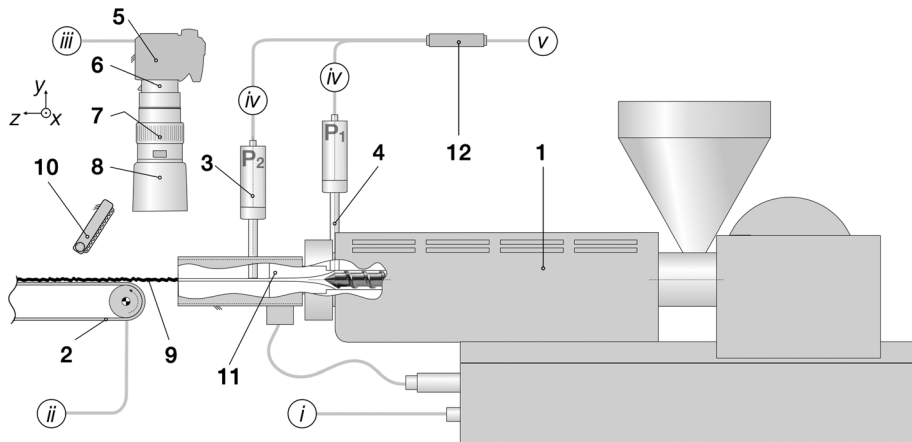


**FIG. 2.** Schematic of the extruder, melt pressure transducers, and inline optical image system: (1) Brabender 19/25D single screw extruder, (2) Brabender conveyor belt, (3) and (4) melt pressure transducers, (5)–(8) inline optical imaging system components, (9) extrudates, (10) LED illumination system, (11) custom extrusion film die, and (12) National Instruments data acquisition board (i, ii, iii, iv, v) commands and control.

pressure at the die entrance in screw-based extruders is the only easily measurable die inlet variable. In this study, the volumetric flow rate  $Q_v$  was obtained from the ratio of extrudate mass flow rate  $\dot{M}$  of collected samples over their proportional densities  $\rho_m$  through Eq. (5). For validation, we then compared the volumetric flow rate thereby obtained with inline optical imaging velocity analysis for 40 wt. % at 21, 66, and 121 rpm.

**III. MODELLING**

To simulate the flow in the film die, the finite element method (FEM)<sup>34</sup> via Comsol Multiphysics 6 (COMSOL, Inc., Stockholm, Sweden) was used. The film die geometry (see Fig. 3) was approximated using computer aided design (CAD) and subsequently imported into Comsol Multiphysics. To decrease the central processing unit (CPU) simulation time, only half of the film die was modeled by applying the

mirror symmetry boundary condition. Simulations were performed on a system with Intel(R) Core(TM) i9-10900 CPU, 128 GB random access memory (RAM), and graphics processing unit (GPU) of 8 GB NVIDIA GeForce RTX 2070 SUPER. The implicit backward differentiation formulas (BDF) time-dependent method along with multifrontal massively parallel sparse direct solver (MUMPS) were used in this study.

**A. Governing equations**

The flow of a polymer melt is governed by the Cauchy momentum equation

$$\frac{Dv}{Dt} = \nabla \cdot S, \tag{7}$$

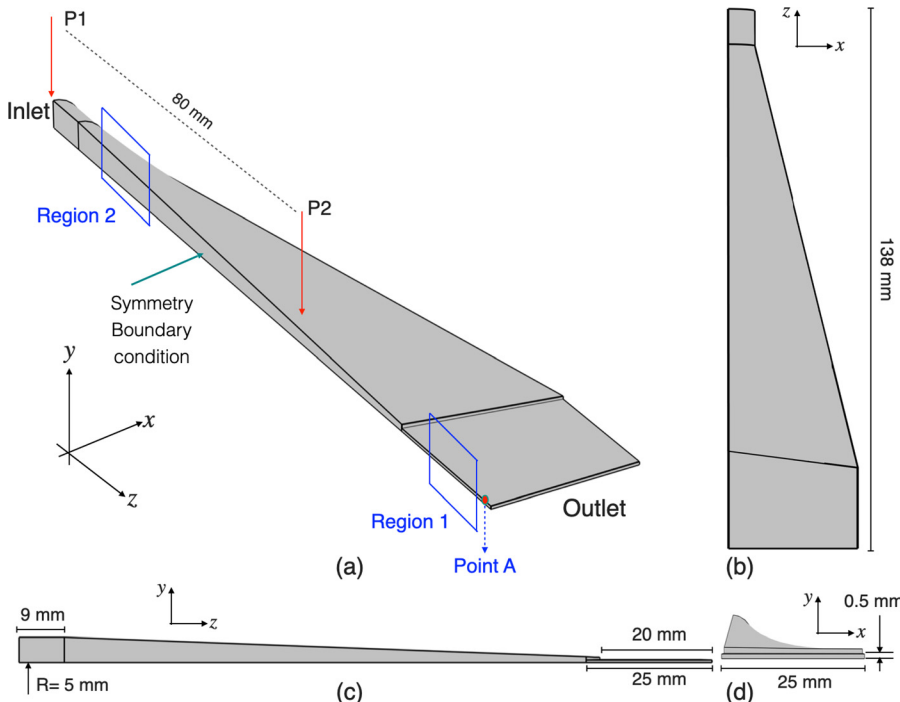


**FIG. 3.** Film die approximate flow geometry: (a) 3D half view of the film die, (b) x–y, (c) y–z, and (d) x–z projections.

26 September 2024 06:35:40

where  $D\mathbf{v}/Dt = \partial\mathbf{v}/\partial t + \mathbf{L}\mathbf{v}$  is the material derivative of the velocity vector  $\mathbf{v}$ ,  $\mathbf{L}$  is the velocity gradient tensor that can be decomposed into the deformation (strain) rate  $\mathbf{D} = 1/2(\mathbf{L} + \mathbf{L}^T)$  and vorticity  $\mathbf{W} = 1/2(\mathbf{L} - \mathbf{L}^T)$  tensors, respectively, and  $\mathbf{S}$  is the total stress tensor. Within the incompressibility assumption, Eq. (7) is complemented by the mass balance equation

$$\text{tr}\mathbf{D} = 0. \tag{8}$$

For a linearly viscous fluid, the total stress tensor in Eq. (7) can be decomposed in an isotropic and extra-stress tensor,

$$\mathbf{S} = -p\mathbf{I} + 2\eta_s\mathbf{D} + \mathbf{T}_f, \tag{9}$$

where  $p$  is the isotropic pressure,  $\eta_s$  is the shear viscosity,  $\mathbf{I}$  is the unit matrix, and the term  $\mathbf{T}_f$  was added to the stress tensor to account for the contributions of the fibers to the total stress. More information about the governing equation of polymer melt can be found in Refs. 35–37. In this study, the extrusion die is equipped with a controlled heating element that helps maintain a constant temperature, compensating for any heat loss and ensuring a stable thermal environment. Thus, the energy equation is not taken into account to reduce the numerical complexity, allowing for a more straightforward analysis of the flow and pressure within the die.

### B. Fiber orientation modeling

The orientation of a single rigid prolate particle in a cartesian reference frame can be described by a vector  $\mathbf{p}$ , see Fig. 4. This vector has a unit length ( $\mathbf{p} \cdot \mathbf{p} = 1$ ), defined as

$$\mathbf{p} = \begin{bmatrix} p_1 \\ p_2 \\ p_3 \end{bmatrix} = \begin{bmatrix} \sin\theta \cos\alpha \\ \sin\theta \sin\alpha \\ \cos\theta \end{bmatrix}. \tag{10}$$

We model the orientation of  $N$  fibers in each mesh element with a second order orientation tensor  $\mathbf{A}_2$  through the average of dyadic products ( $\mathbf{p}\mathbf{p}$ ) of  $N$  fibers,

$$\mathbf{A}_2 = \mathbf{p}\mathbf{p} = \frac{1}{N} \sum_{k=1}^N (\mathbf{p}\mathbf{p})_k. \tag{11}$$

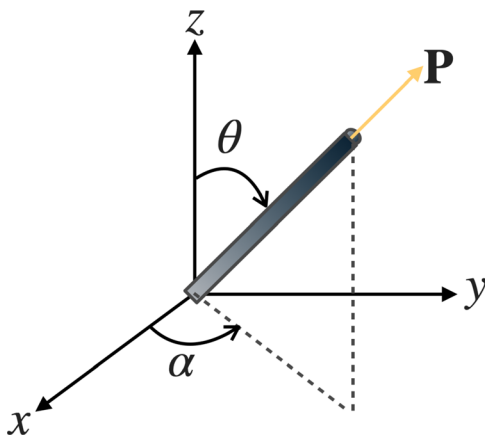


FIG. 4. Orientation of a single fiber defined by  $\mathbf{p}$  vector in the Cartesian coordinate.

Thus, the fiber component of the extra-stress tensor in Eq. (9) can then be expressed as

$$\mathbf{T}_f = 2\eta_s N_p (\mathbf{D} : \mathbf{A}_4), \tag{12}$$

where the “:” operator is the double dot product  $\mathbf{D} : \mathbf{A}_2 = \text{tr}(\mathbf{D}\mathbf{A}_2^T) = D_{ij}A_{ji}$ ,  $N_p$  is the so-called particle number, a dimensionless term that represents the relative importance of the fibers,  $\mathbf{A}_4$  is a fourth order orientation tensor, and  $\phi_{vol}$  is commonly determined from the rule of mixtures Eq. (6) as follows:

$$\phi_{vol} = \frac{\rho_{mc} - \rho_{mp}}{\rho_f - \rho_{mp}}. \tag{13}$$

According to the model derived by Dinh and Armstrong,<sup>39</sup> particle number ( $N_p$ ) can be approximated for semi-concentrated composites with random fiber spacing as

$$N_p \approx \frac{\phi_{vol}(L/D)^2}{3 \ln[(\pi D)/(2\phi_{vol}L)]}. \tag{14}$$

There are different closures to approximate  $\mathbf{A}_4$ , such as linear,<sup>40</sup> quadratic,<sup>41</sup> hybrid,<sup>42,43</sup> eigenvalue based orthotropic fitting,<sup>44</sup> and invariant based orthotropic fitting.<sup>45</sup> In this study, the quadratic closure approximation was implemented, where  $A_{ijkl} \approx A_{ij}A_{kl}$ . Thus, Eq. (12) can be re-written as

$$\mathbf{T}_f = 2\eta_s N_p [(\mathbf{D} : \mathbf{A}_2)\mathbf{A}_2]. \tag{15}$$

Finally, Eqs. (7), (8), (11), and (15) can be coupled to the Folgar–Tucker diffusive term<sup>27</sup> to consider fiber–fiber interactions. However, particle orientation dynamics have been shown to be much faster numerically than experimental results have shown.<sup>38,46</sup> Therefore, in this study, to scale the numerical orientation time to the experimental orientation time, a strain reduction factor (SRF)  $\kappa$  method<sup>47</sup> was taken into account, as follows:

$$\dot{\mathbf{A}}_2 = \frac{D\mathbf{A}_2}{Dt} = \kappa[\mathbf{W} \cdot \mathbf{A}_2 - \mathbf{A}_2 \cdot \mathbf{W} + \zeta(\mathbf{D} \cdot \mathbf{A}_2 + \mathbf{A}_2 \cdot \mathbf{D} - 2\mathbf{D} : \mathbf{A}_4) + 2C_I|\dot{\gamma}|(\mathbf{I} - 3\mathbf{A}_2)], \tag{16}$$

where  $\kappa$  is a strain reduction factor that increases the orientation time of particles in flow. The strain reduction factor (SRF) is equivalent to the slip parameter proposed by Sepehr *et al.*<sup>46</sup> in 2004. More information about SRF and its influence on orientation can be found in Refs. 47–50, where  $\zeta$  is a function of fiber aspect ratio ( $L/D$ ),  $\zeta = ((L/D)^2 - 1)/((L/D)^2 + 1)$ ,  $|\dot{\gamma}|$  is the effective deformation rate (square root of the second invariant of the strain rate tensor). In this study, the constant  $C_I$ , also known as interaction coefficient (CI), was approximated using the expression of Bay,<sup>51</sup> whereby

$$C_I = 0.0184 \exp[-0.7148 \phi_{vol}(L/D)]. \tag{17}$$

This empirical relationship for CI allows for a more accurate prediction of fiber orientation, especially in concentrated suspensions where fiber interactions are significant. The exponential decay form of CI effectively captures the influence of fiber volume fraction and aspect ratio, leading to better alignment with experimental observations. According to the Jeffery model, every particle under shear is oriented eventually in the flow direction. The addition of the strain reduction

factor to the equations governing fiber motion results in a loss of material objectivity of the equation; however, in this study, due to the dominance of shear flows (deformation to vorticity), furthermore to simplify the three-dimensional CFD model, we avoid using other advanced eigenvalues-based models such as reduced strain closure (RSC), or retarding principle rate (RPR).<sup>48</sup>

**C. Boundary, initial conditions, and material functions**

The Dirichlet boundary condition using volumetric flow rate obtained from experimental results (Table SI1) was applied at the die entrance (inlet), see Fig. 3. An isotropic Dirichlet boundary condition accounting for a random orientation at the inlet was implemented at the entrance of the geometry as follows:

$$A_{ij} = \begin{cases} 1/3 & \text{if } i = j, \\ 0 & \text{if } i \neq j. \end{cases} \quad (18)$$

No slip, and Navier slip<sup>52</sup> boundary conditions with slip lengths from capillary rheometry were applied on the walls. The isotropic pressure was set to zero at the exit of the die. The initial values for the velocity vector components and pressure were set to 0. The initial conditions for the orientation tensor were also set isotropically, Eq. (18). As material functions, power-law functions fitted to the capillary rheometry data together with the melt density estimations also from capillary rheometry were used as material functions.

**IV. QUANTITATIVE ESTIMATION OF FIBER ORIENTATION**

The composite morphology and observations of fiber orientation in the matrix were carried out using a scanning electron microscope (SEM; Philips XL-30 ESEM, The Netherlands). The planar section of the samples (regions 1 and 2, Fig. 15) was polished, and gold-sputtered prior to SEM. Obtained SEM micrographs were stitched together to extend the visualization area. Subsequently, the micrographs were imported to Matlab R2021b and analyzed using a custom code based on the so-called method of ellipses. In the method of ellipses, the fibers are initially fitted with ellipses, followed by measuring the angle at which the ellipses are oriented, see Secs. IV A and IV B. In addition, fibers according to their orientation angle were filled with different colors. Furthermore, the data from numerous fibers were averaged to estimate the orientation tensor quantitatively.<sup>38</sup>

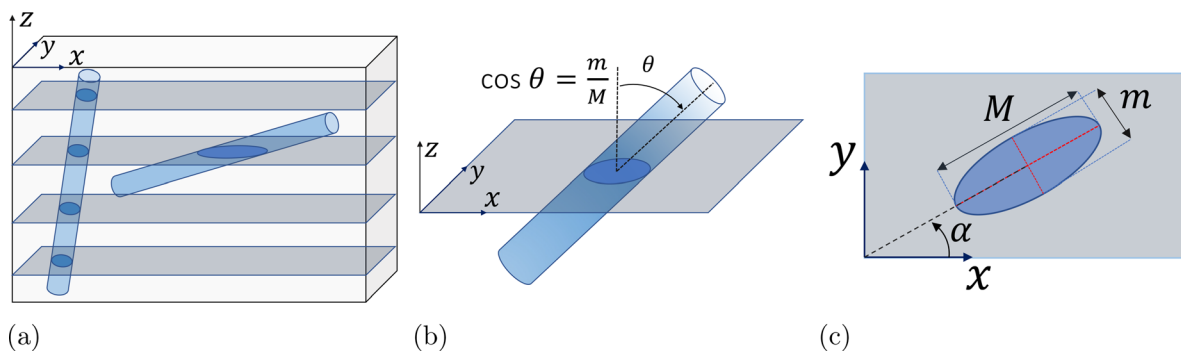


**FIG. 5.** Sectional view for determining fiber orientation based on imaging analysis: (a) 3D sectional illustration of fibers in the matrix, (b) 3D illustration of one single fiber crossing a plane, and (c) 2D top view of fiber cross section on the xy plane.

**A. Mathematical background**

The principle behind fiber orientation measurement is depicted in Fig. 5. In the figure, the x-y plane refers to the section plane. The cross section of the fibers is in the form of an ellipse with the major and minor axes  $M, m$  and  $\alpha, \theta$  are azimuthal and polar orientation angles of the fiber.

The orientation vector  $\mathbf{p}$  can be estimated from Eq. (10) and the second-order orientation tensor  $\mathbf{A}_2$  can be calculated from Eq. (11). An unbiased average can be obtained by dividing the fiber's contribution to its projected length and normalizing it,<sup>38</sup>

$$A_{ij}^w = \frac{\sum_{k=1}^N (p_i p_j)_k / (l \cos \theta_k)}{\sum_{k=1}^N 1 / (l \cos \theta_k)}, \quad (19)$$

where  $l$  denotes the length of the fiber, and the angle of orientation of the fiber with respect to the section plane is  $\theta$  and is given by:  $\cos \theta = m/M$ . Equation (19) is further simplified, and subsequently, the unbiased average for the second order orientation tensor<sup>53</sup> can be calculated as

$$A_{ij}^w = \frac{\sum_{k=1}^N (p_i p_j)_k W_k}{\sum_{k=1}^N W_k}, \quad (20)$$

where  $W_k = \frac{1}{\cos \theta_k}$  is weighting function.

**B. Image analysis**

SEM micrographs were analyzed using a custom Matlab code. Due to the limited observation area, individual images corresponding to small portions of the sample surface were captured and were stitched together in a composite image. The composite images were imported into the MATLAB code, filtered, and binarized. The binary images were then fitted with an equivalent ellipse around the fiber boundaries and in-built functions in MATLAB were utilized to extract the ellipse parameters. Upon calculating the ellipse parameters, the weighting function  $W_k$ , and second order orientation tensor  $A_{ij}^w$  was estimated using Eq. (20).

**V. RESULTS AND DISCUSSION**

**A. Melt density**

Melt densities of WPCs at 180 °C are shown in Fig. 6. It can be observed that the addition of wood fiber to the matrix increases the



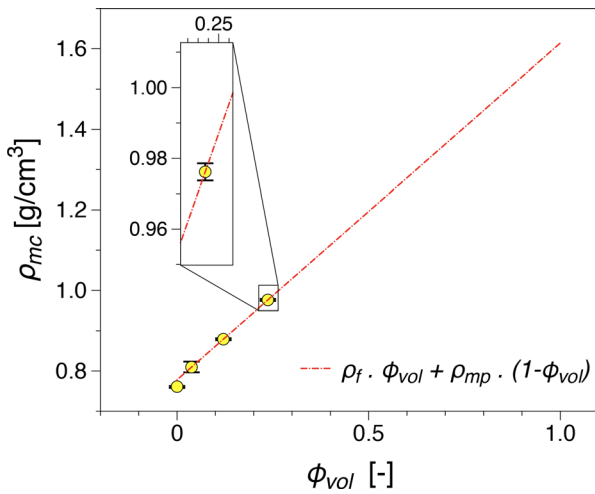


**FIG. 6.** WPCs melt densities at  $T = 180\text{ }^\circ\text{C}$  as a function of wood fiber volume fraction in Polypropylene. The dashed line represents Eq. (6) with  $\rho_{mc} = 1.61 \cdot \phi_{vol} + 0.778(1 - \phi_{vol})$ .

melt densities of composites linearly, and the densities are fitted with a generic equation of the form Eq. (6) showing that the rule of mixtures appears valid. By extrapolating to the  $\phi_{vol} = 0$  (unfilled) and  $\phi_{vol} = 1$  limits, the densities of the polypropylene melt and the wood fibers can be estimated as  $\rho_{mp} = 0.77\text{ g/cm}^3$  and  $\rho_f = 1.61\text{ g/cm}^3$ .

**B. Viscosity, wall slip, and slip length functions**

The shear thinning region ( $\dot{\gamma}_a > 30\text{ 1/s}$ ) of the shear viscosity functions, Fig. 7(a), was fitted with the power-law model, Eq. (1), to obtain the slip velocity ( $V_s$ ) using Eq. (2). Fitting parameters for all materials are listed in Table I. Slip velocities as a function of shear stress and shear rate are shown in Figs. 7(b) and 7(c), respectively. A more extensive discussion on the rheological properties of the WPCs as well as their implication for processing can be found elsewhere.<sup>7</sup>

Slip velocities in the investigated WPCs are significant, e.g., for 40 wt. % at a shear rate of 600 1/s, the slip velocity constitutes  $\sim 40\%$  of the average flow velocity. The slip length,  $b$ , as a function of the no-slip shear rate,  $\dot{\gamma}_{ns}$ , obtained from Eq. (3) is shown in Fig. 7(d). As mentioned in Sec. II A 1, two scenarios for slip lengths are considered in the simulations. For the first scenario, we assume the slip length to be constant and equal to the maximum slip length for each composition

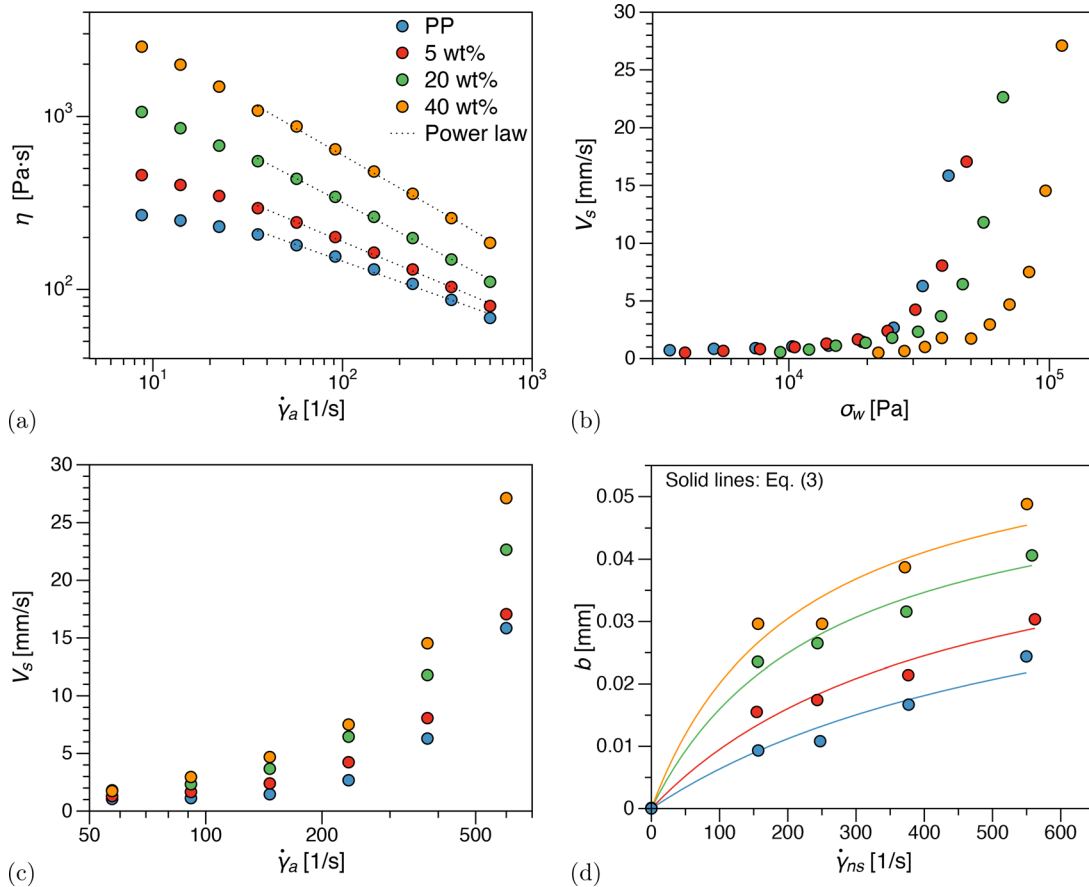


**FIG. 7.** Capillary rheometry results at  $T = 180\text{ }^\circ\text{C}$ : (a) viscosity vs shear rate, (b) slip velocity vs wall shear stress, (c) slip velocity vs shear rate, and (d) slip length obtained from Eq. (3).

26 September 2024 06:35:40

**TABLE I.** Fitting parameters for the viscosity functions in Fig. 7(a) using the power-law model, Eq. (1), at 180 °C.

	PP	5 wt. %	20 wt. %	40 wt. %
$n$	0.607	0.540	0.429	0.368
$K$	886.86	1572.25	4387.49	10 951.87
$b_{const}$ (mm)	0.022	0.028	0.04	0.05

obtained from capillary rheometry measurements, Fig. 7(d). The slip lengths are listed in Table I. For the second scenario, we impose a shear rate dependent slip length, by fitting Eq. (4) to the data in Fig. 7(d) (solid lines). The obtained fitting parameters are listed in Table SI1 (supplementary material). While  $b_{max}$  increases with the addition of wood fiber to the matrix,  $\dot{\gamma}_c$  decreases, which means that by increasing the fiber concentration, the transition from  $b_{min}$  to  $b_{max}$  occurs at lower shear rates.

**C. Inlet velocity**

Die inlet average velocities obtained from mass flow rate measurements are compared with velocities obtained from inline imaging analysis for 40 wt. % fiber content at three different screw speeds (21, 66, and 121 rpm) in Fig. SI5(a) (Sec. SI7). The extrudate velocities are averages of three points along the extrudate width at exit ( $w_1$ ,  $w_2$ , and  $w_3$ ); see Fig. SI5(b). The full set of data obtained can be found in Table SI2. It can be observed that at lower wood fiber concentrations, differences between  $w$  obtained through mass flow rates and inline imaging are considerable; however, by the addition of wood fiber  $w$ , differences diminish. The main reason for these differences is die swelling phenomena. Lower concentrations and neat PP have more swelling compared to higher concentrations, and therefore velocities obtained through inline imaging were underestimated. Hence, for numerical simulations, velocities obtained through mass flow rate were used, as

velocities obtained from image analysis could be tainted with errors due to the die-swelling.

**D. Mesh optimization**

A fully structured mesh generated for the die flow geometry having a Skewness quality factor (see Sec. SI3) of 0.812, is shown Fig. 8. To assess the quality of the mesh, we have studied the influence of the total number of elements on the velocity profile in section B-B in Fig. 8(a). The optimization was done using material data for PP at 21 rpm. Several total number of elements, 9900, 44 000, 110 656, and 181 200, were examined. According to the mesh convergence tests in Fig. 8(b), velocity profiles with 110 656, and 181 200 are very close to each other with a standard deviation error of 0.8%; hence, the rest of the simulations were done using 110 656 elements. Velocity profiles as a function of  $y$ -coordinate are shown in Fig. 8(b).

**E. Numerical and experimental pressures**

The pressure contours for a melt with 20 wt. % fiber content at 66 rpm with no-slip boundary condition is illustrated in Fig. 9. Simulated pressure data along the A-A section ( $z$ -coordinate), were extracted for comparison with pressure transducers (experimental) data, see Fig. 10. For all cases, pressure gradients are nonlinear from the die inlet ( $z=0$  mm) to the contraction ( $z=113$  mm), due to expansion/contraction characteristics of the film die. However, after the contraction ( $z > 113$  mm), due to the constant thickness in the die, pressure decreases linearly with  $z$ . During the experiment, the pressure data were constantly monitored, and enough time was given at each screw speed to see when the flow reached a steady state; Pressure data obtained from transducers as a function of time for all cases can be seen in Fig. SI7.

Figure 10(a) shows pressure rise with the addition of wood fiber compared to the neat PP due to the incorporation of higher shear viscosities of highly filled composites. In addition, influence of screw speed on pressure results is shown as an example for 20 wt. % in

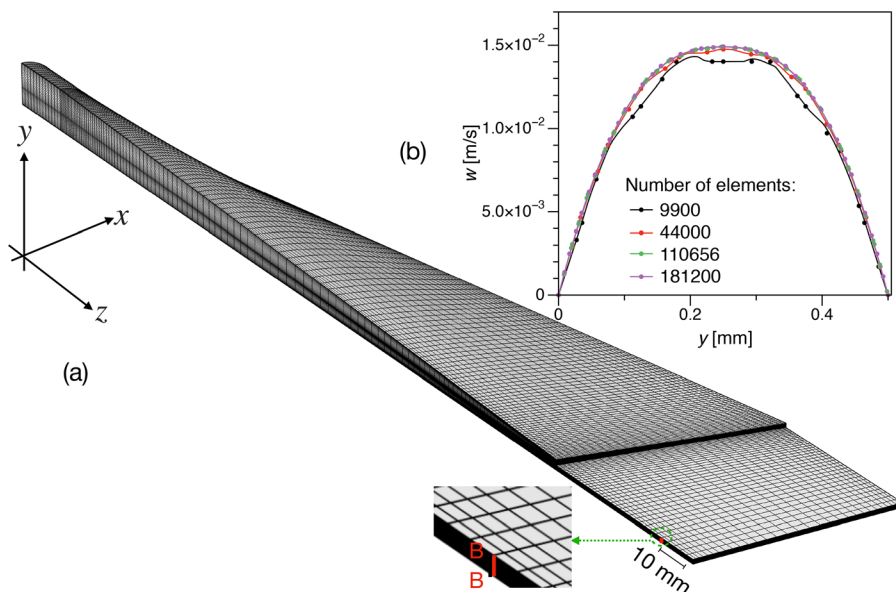


**FIG. 8.** (a) Example of mesh structure and (b) influence of the total number of mesh elements on the velocity profile.

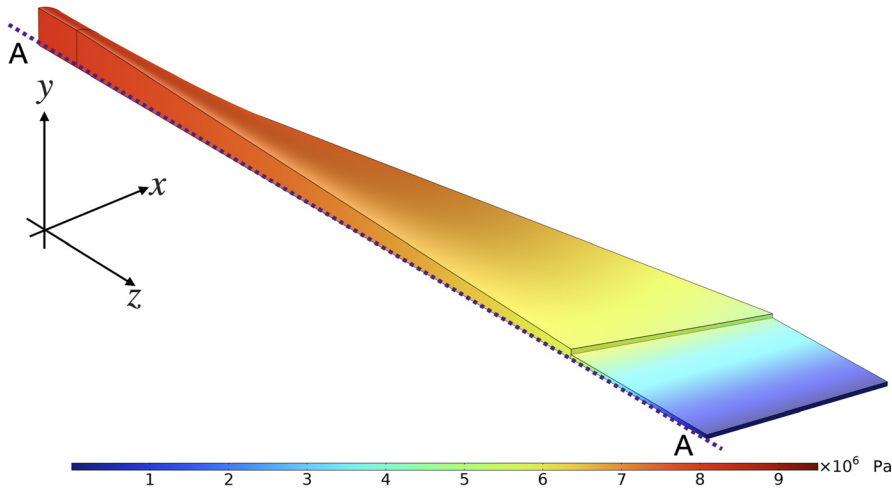


FIG. 9. Isotropic pressure contours for 20 wt. % at 66 rpm.

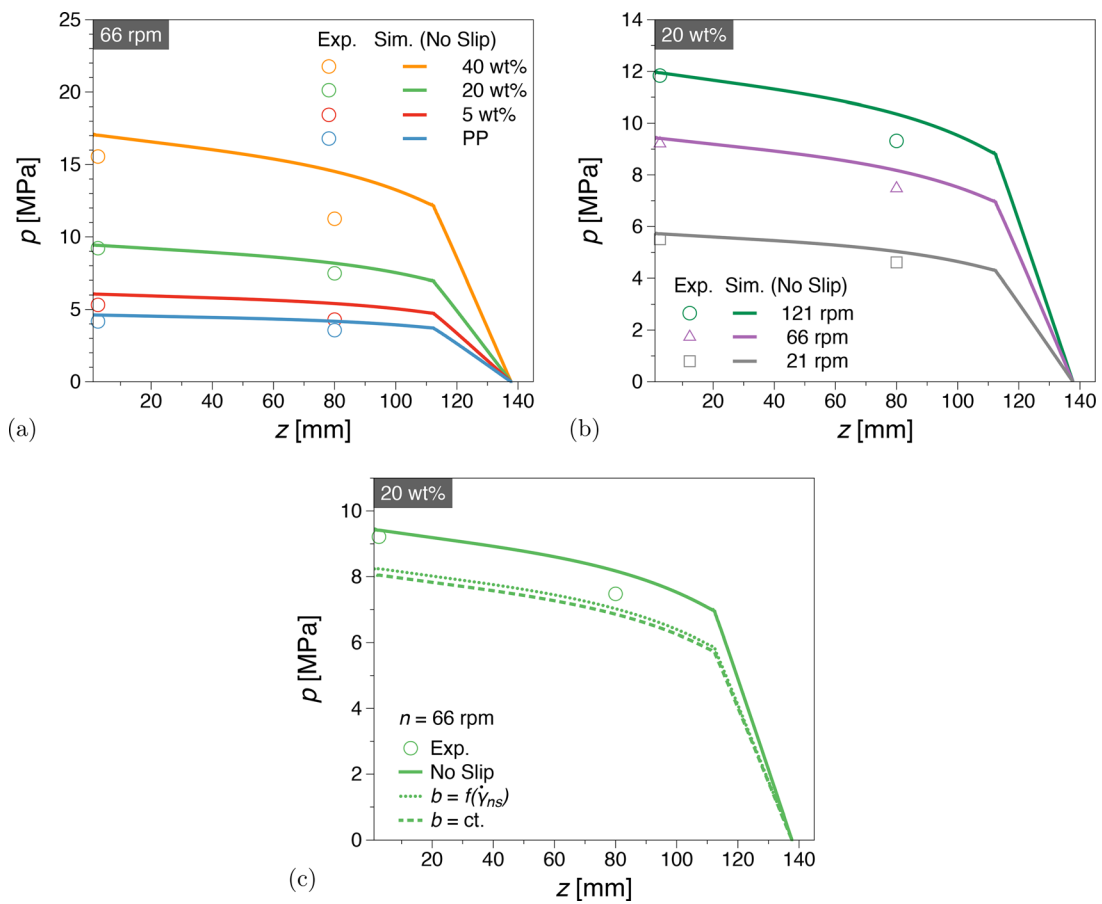


FIG. 10. Pressure results obtained along the A-A section (in Fig. 9) numerically vs determined (mechanical) pressure experimentally at  $T = 180\text{ }^\circ\text{C}$ : (a) influences of wood fiber content on pressure at  $n = 66\text{ rpm}$ , (b) influences of screw speed on pressure for 20 wt. %, and (c) influences of slip on pressure for 20 wt. % at  $n = 66\text{ rpm}$ .

26 September 2024 06:35:40

Fig. 10(b). Applying wall slip velocity boundary conditions causes a pressure drop for all concentrations and all screw speeds, as expected. For instance, for 20 wt. % at 66 rpm, slip length effects can be observed on pressure obtained from simulations in Fig. 10(c), where the pressures obtained with constant slip length ( $b = ct.$ ) are always lower than pressure with variable slip length  $b = f(\dot{\gamma}_{ns})$ . This is due to the overestimation of slip impact on the flow and considering the maximum slip length as the constant  $b$ . Effects of filler content, screw speed and slip boundary conditions on pressure and slip velocities along the AA section are represented in Figs. S18(a) and S18(b) thoroughly. Based on Fig. S18(b), slip velocities with constant  $b$  are always higher than variables  $b$  Fig. S18(b) shows that the increase in wood fiber content increases slip velocities. It can be observed that from the die inlet ( $z = 0$  mm) toward the contraction/expansion region where ( $0 < z < 113$  mm) velocities increase, and at the contraction  $z = 113$  mm, a significant sudden velocity increase occurs due to the contraction and higher shear rates at the die exit. Moreover, Fig. S18(b) shows that for all compositions by increasing screw speeds, the difference between slip velocities of variable slip lengths  $b = f(\dot{\gamma}_{ns})$ , and constant slip lengths ( $b = ct.$ ) reduces. The reduction is more evident at higher fiber concentrations (20 and 40 wt. %). Similar behavior can be seen in the pressure results Fig. S18(a), where at 121 rpm, pressures

obtained through constant  $b$ , and variable  $b$  are very close to each other. The aforementioned characteristics are due to the correlation between higher shear rate/higher screw speed and the transition shear rate ( $\dot{\gamma}_c$ ) in Eq. (4), where due to the inclusion of higher shear rates at higher screw speed, variable slip length  $b$  pass the transition shear rate ( $\dot{\gamma}_c$ ) rapidly, and ends up at upper limit of the slip length ( $b_{max}$ ), see also Figs. 11 and S19. In two figures mentioned, the  $x$  axes represent the screw speeds, and the  $y$  axes represent error or deviation of simulation pressures from the experimental results:  $Error = (|p_{sim} - p_{exp}|) / p_{exp} \cdot 100\%$ .

For PP at  $z = 80$  mm, it can be observed that the errors with considering constant slip length, at 21 and 66 rpm are lower than their counterparts with variable slip length. According to the viscosity functions in Fig. 7(a), PP does not obey the power-law model at lower screw speed/shear rates; hence we expected an overestimation in pressure to occur for [ $b = f(\dot{\gamma}_{ns})$ ] in Fig. 11(a). However, for  $b = ct.$  cases, the pressure overestimation at lower shear rates was counteracted by the slip length overestimation. Thus, the error at  $z = 80$  mm at 21, and 66 rpm for constant slip lengths are lower than the similar case studies with variable slip lengths.

For 5 wt. % fiber content at  $z = 80$  mm, Fig. 11(b), a similar trend to PP can be observed, where at lower screw speeds, the error is higher

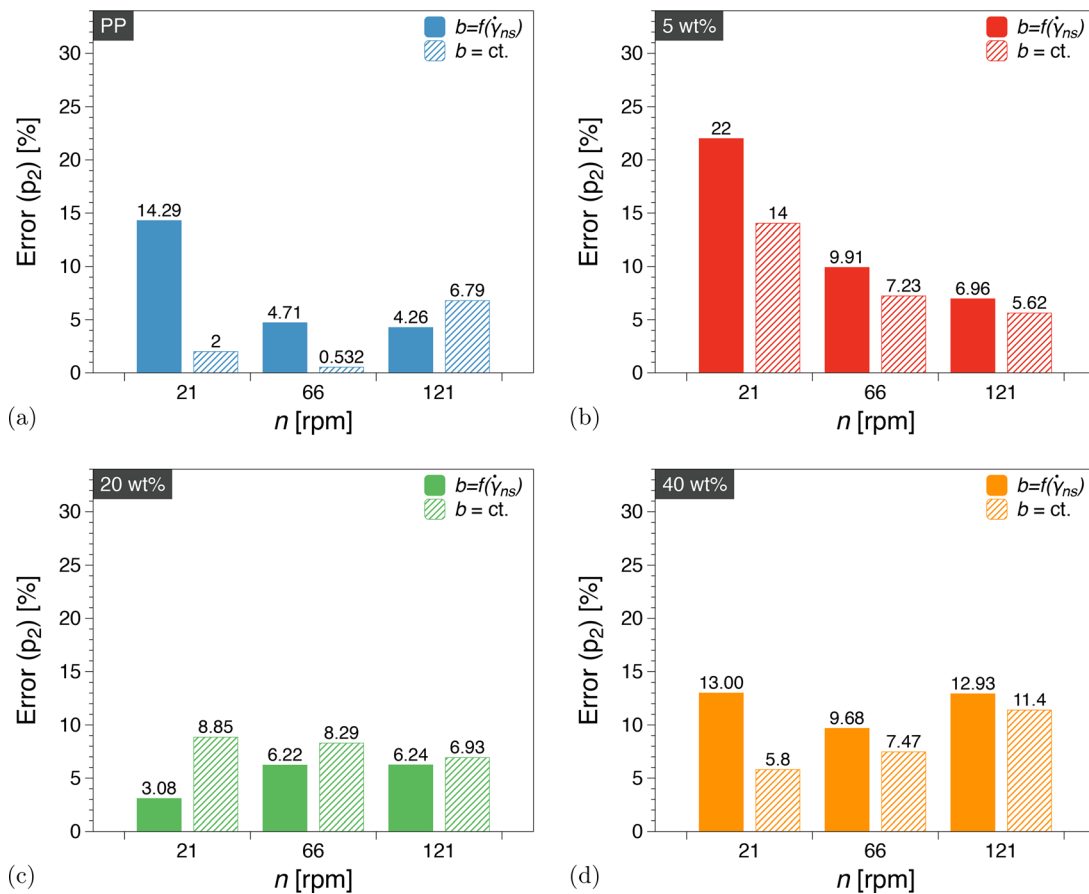
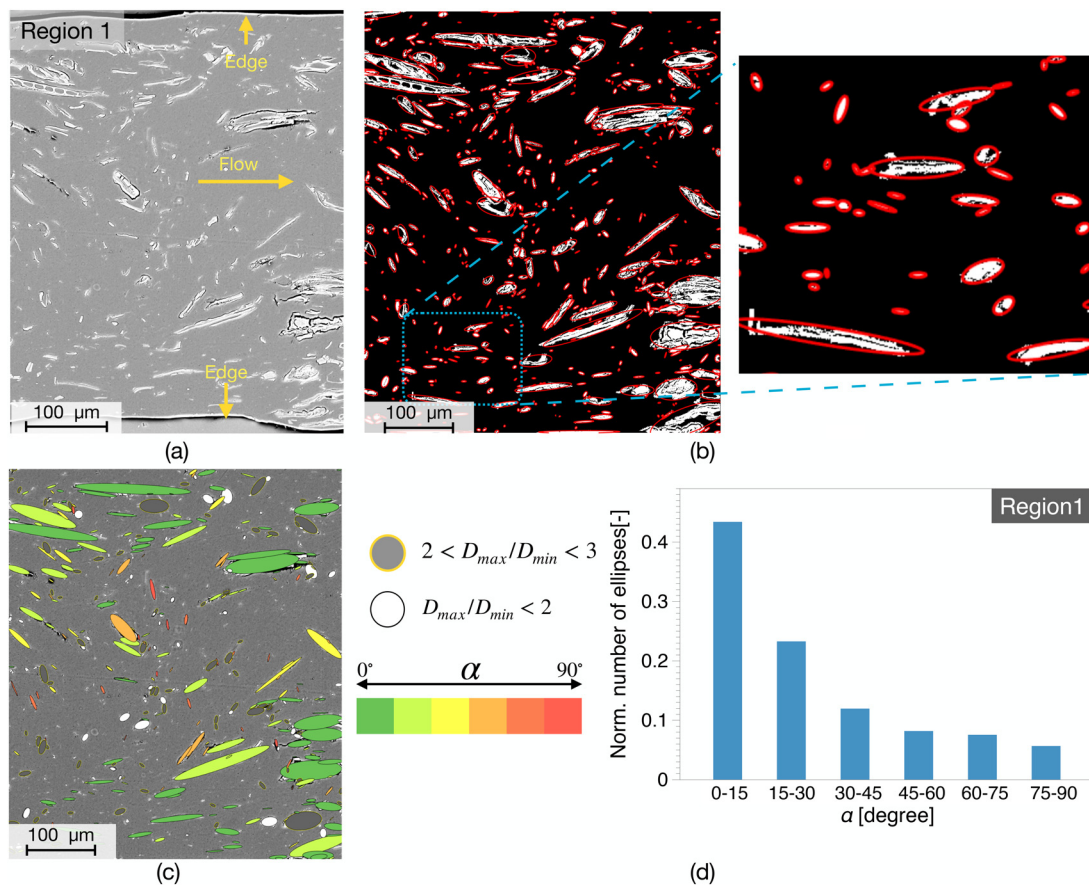


FIG. 11. Comparison between the numerical isotropic pressure along the A–A section in Fig. 9 at  $z = 80$  mm and mechanical pressure ( $p_2$ ) determined experimentally in terms of relative error, with constant slip length ( $b = ct.$ ), and variable slip length  $b = f(\dot{\gamma}_{ns})$ : (a) PP, (b) 5 wt. %, (c) 20 wt. %, and (d) 40 wt. %.



**FIG. 12.** Experimental analysis of orientation from SEM micrographs in Region 1: (a) example of SEM for 20 wt. % extruded at 66 rpm and  $T = 180^\circ\text{C}$ , (b) fitting of fibers with ellipses, (c) color-coded orientation figure, and (d) histogram of orientation angle.

due to errors associated with applying the power-law model at lower shear rates. In addition, at 121 rpm, due to the high shear rates and similar slip lengths, the errors are similar.

For 20 wt. % fiber content, since the power-law model can be fitted over a broader range of data points due to the dominant shear thinning behavior [Fig. 7(a)], and consequently, simulations could lead to lower errors, see Fig. 11(c). In addition, it can be observed from Fig. S18(a) that pressures obtained through simulations are lower than the experimental pressure. Three factors could influence on the underestimation of the pressures. First, the slip lengths on the walls for both case studies, due to the simplifications in measuring wall slip velocity using Mooney method, are overestimated. Second, the power-law model implies difficulties in the constitutive modeling at low shear rates and overall the generalized Newtonian constitutive framework excludes elastic contributions to the total stress. Normal stresses are thus not present in the simulations but would be measured by the melt pressure sensors. We briefly note that melt-pressure transducers provide a “mechanical” pressure which is a contribution of both the isotropic pressure and normal stresses.<sup>54</sup> Finally, the temperature within the flow domain may not be uniformly distributed. Particularly at higher rpm, specific regions within the domain may exhibit temperatures lower than  $180^\circ\text{C}$  and since the energy equation and thermal

dissipation are neglected in this study, the temperature variation can result in increased viscosities, leading to higher pressures.

For 40 wt. % fiber content, Fig. 11(d), the error is slightly higher compared to 20 wt. %. Similar to the other compositions, the errors in the case of  $b = ct$ , are lower due to the higher slip lengths. Upon comparing the error shown in Fig. 11(d) with Fig. S18(a), it is evident that the simulated pressures are higher than the experimental mechanical pressure. The aforementioned differences can be attributed to two factors. First, it is possible that the actual slip lengths are higher than the implemented values and second, it should be acknowledged that WPCs with a fiber content of 40 wt. % could contain improper filling regions within the die. Since the simulations were conducted under the assumption of a filled die, the resulting simulation pressures could therefore be overestimated.

The pressure error, Fig. S19, shows differences between simulations and experiments at the die inlet. Pressure errors are lower for variable slip lengths than for constant slip lengths. In detail, 20 and 40 wt. % fiber content and at all screw speeds with constant slip lengths, the pressure error is higher due to overestimation of slip. For 5 wt. % fiber content and for neat PP, the error due to power-law model limitations is higher. Several factors could lead to the error and inconsistency: (1) the simplification of the geometry in the simulation at the inlet; (2) the

true position of the first transducer where the first transducer was placed before the die and adaptor, thus, the contraction in the adaptor, the distance between the inlet of the die and transducer position, and (3) thermal effects could cause the inconsistency.

### F. Experimental determination of fiber orientation

SEM micrographs in Region 1 of the materials extruded (see Fig. 3) are presented in Fig. 12. Fitted ellipses are shown in Fig. 12(b), as described in Sec. IV. Fibers can break due to the high wall shear stress between the screw and the barrel during extrusion, ellipse fitting on the SEM of Region 1 [Fig. 12(a)] indicates a significant decrease in the length and diameter of fibers, for more information on size of fiber see Fig. S14. Orientation analysis from the elliptical shape fitting in Fig. 12(b) is represented as color-coded images in Fig. 12(c) and as a normalized histogram in Fig. 12(d). It can be determined from the results that a large proportion of the fibers (more than 40%) are oriented at angles between  $0^\circ$  and  $15^\circ$ . This indicates the strong alignment of the fibers along the flow direction in Region 1, where the nominal shear rate is comparatively high. Additionally, from the color-coded SEM micrographs, it is apparent that the fibers present close to

the wall have a preferential orientation toward the flow compared to those farther away from the wall. In Fig. 12(c), fibers with  $D_{max}/D_{min} < 3$  are colored in white, and gray as the minimum aspect ratio observed for a single fiber in our sample was four according to our initial SEM analysis. Therefore, ellipses with an aspect ratio  $< 3$  have to be perpendicular or tilted to the surface. We can also not exclude the presence of complex fiber morphologies, such as fiber bundles, agglomerates, etc. Concurrently, it can be observed that in the central part of the SEM micrograph in Fig. 12(c), the fraction of particles perpendicular or tilted is more significant than in the regions close to walls.

A similar analysis was done for Region 2 (see Fig. 3) where, Fig. 13 illustrates SEM micrographs, fitted ellipses, and histogram depicting the angles at which the fibers are oriented. The results show that fibers in Region 2 are less oriented in the flow direction when compared to Region 1 as expected. The proportion of fibers aligned in the flow direction in Region 2 is  $\sim 30\%$  as opposed to nearly 45% in Region 1. However, similar to Region 1, a greater amount of fibers were oriented in the flow direction at the walls compared to the middle section. It is also noticeable that in Fig. 13(c), more fibers perpendicular to the surface and flow (filled with white and gray colors) can be observed.

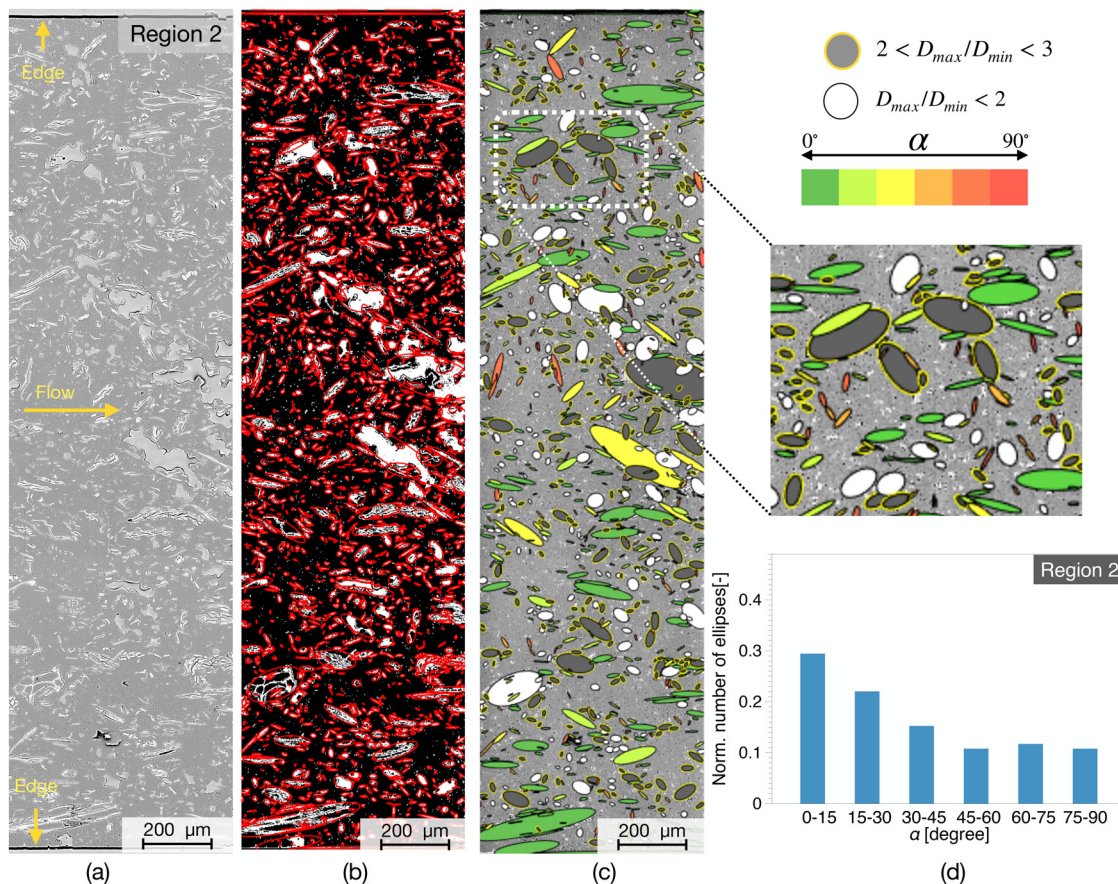


**FIG. 13.** Experimental analysis of orientation from SEM micrographs in Region 2: (a) example of SEM for 20 wt. % extruded at 66 rpm and  $T = 180^\circ\text{C}$ , (b) fitting of fibers with ellipses, (c) color-coded orientation figure, and (d) histogram of orientation angle.

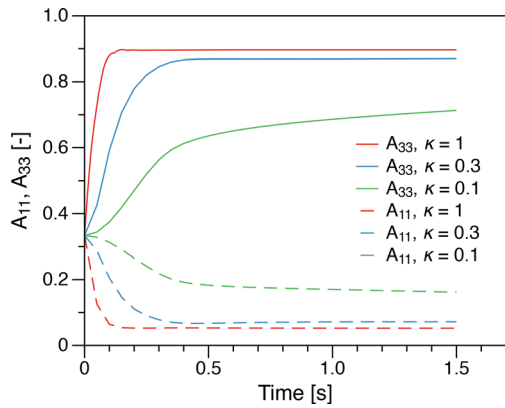


FIG. 14. Effect of strain reduction factor (SRF) on  $A_2$  components of the point A shown in Fig. 3.

G. Orientation from numerical modeling

1. Effect of strain reduction factor

The effect of the strain reduction factor (SRF), see Eq. (16), on the orientation tensor components, see Eq. (11), is highlighted in Fig. 14 for (fixed) point A in Fig. 3. Preliminary numerical investigations were performed to optimize SRF with respect to the experimental results (described ahead). According to our initial interpretation with  $\kappa = 1$ , and  $\kappa = 0.3$ , fibers orient comparatively fast, and the resulting orientations were not matching experimental observations.<sup>38,46,47</sup> In contrast,  $\kappa = 0.1$ , showed a better agreement with experimental results.

Time is another vital factor that could influence on  $A_2$  components. According to Jeffrey’s fiber orientation model, fibers in the flow, influenced by shear, eventually orient in the flow direction. In other

words, Jeffrey model is time-dependent, which means all the fibers could be oriented in the flow direction with the evolution of time. Hence, selecting an acceptable time for analysis and validation purposes is important. To select the right time,  $A_{33}$  obtained through SEM in Region 2, is compared to  $A_{33}$  obtained through modeling at different times in Fig. SI10. Based on the comparison done, Time = 1 s is selected for the upcoming validations.

2. Fiber orientation distribution

Fiber orientation distribution in the entire flow domain for 20 wt. % fiber content at 66 rpm (Time = 1 s) considering variable slip length is illustrated by the first eigenvalue/eigenvectors of the orientation tensor  $A_2$  in Fig. 15. The colormap in Fig. 15, represents the first eigenvalue, and the arrows stand for the first eigenvectors. Along the y-direction for a core region, the first eigenvalues are smaller, which means there is weak orientation in the flow (z) direction. This is in contrast to regions close to the walls where the fibers are subjected to the highest local shear rates, i.e., greater eigenvalues, and consequently, exhibit stronger orientation in the flow (z) direction.

H. Experimental validation of the numerical orientation distribution function

Figure 16 shows the numerical prediction of fiber orientation in detail and the comparison of the orientation distribution from the obtained  $A_2$  tensors in selected Region 1 and Region 2 (marked in Fig. 2), to the distribution of orientation tensors  $A_2$  calculated through SEM image analysis (as described in Sec. IV).

Figure 16(a) represents the  $A_2$  first eigenvalues contour and velocity profiles in Region 1, and Fig. 16(b) shows the numerical, experimental  $A_2$ , and velocity in the flow direction as a function of y. At the core of the flow domain in Fig. 16(a), here  $y = 0.25$ , it shows a

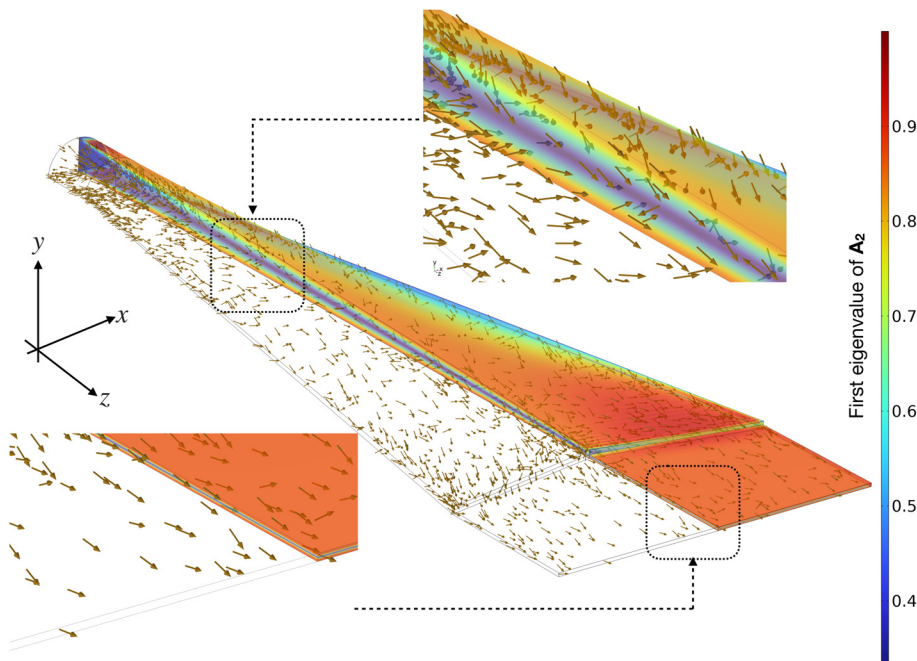
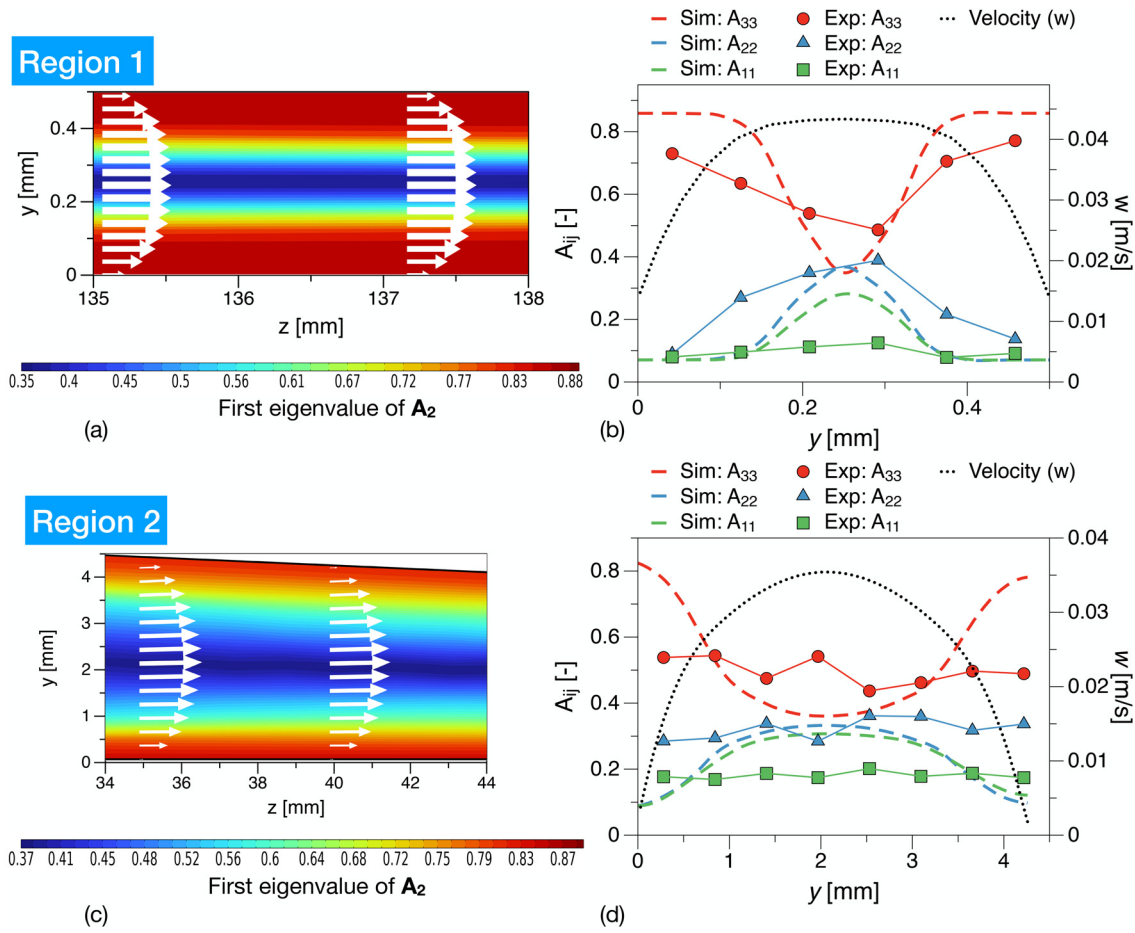


FIG. 15. First eigenvalues and eigenvectors of the orientation tensor  $A_2$  for 20 wt. % at 66 rpm.

26 September 2024 06:35:40



**FIG. 16.** Comparison between experimental and numerical fiber orientation for 20 wt. % at 66 rpm, considering variable slip lengths, Time = 1 s,  $T = 180^\circ\text{C}$  in Regions 1 and 2: (a) first eigenvalue in Region 1, (b)  $A_2$ , and velocity as a function of  $y$  for Region 1, (c) first eigenvalue in Region 2, and (d)  $A_2$ , and velocity as a function of  $y$  for Region 2.

random orientation. The orientation tensor  $A_2$  components, numerically and experimentally express a stronger degree of orientation in areas closer to the walls, due to the higher local shear rates and isotropic orientation in  $0.15 < y < 0.35$ , due to lower shear rates, where the velocity  $[w(x, y)]$  distribution reaches a plateau comparatively. Not only do the two agree qualitatively, but also quantitatively, except for  $A_{11}$ . The spatial distributions in  $A_{33}$  and  $A_{22}$  seem broader than the numerical counterparts. Consequently, this could imply that the experimental velocity gradient might exhibit significant local shear rate gradients, but these gradients are likely confined to a limited region near the walls. Several reasons for these differences between simulation and experimental findings could be inferred. Due to the simplifications in the modeling, for example, the energy equation, heat dissipation, were not considered in this study; in addition we implemented SRF method instead of RSC or other approaches which can cause this error. Another contributing factor could be the assumption of incompressibility for the simulated materials. In practical scenarios, these materials might exhibit compressibility under high pressure conditions. Finally, when quantifying the orientation tensor  $A_2$ , we assumed that the fibers are uniform and rigid; however, in reality they possess both flexibility and non-uniformity.

A similar analysis was done for Region 2 (see Fig. 3) where, Figs. 16(c) and 16(d) illustrate fiber orientation with first eigenvalues, and  $A_2$  components, respectively. Results show that compared to Region 1, fibers in Region 2 are less oriented in the flow direction. In other words, Figs. 16(c) and 16(d) show that the isotropic core is broader compared to Region 1, due to the velocity profile, and lower shear rates in Region 2. Both experimental and numerical results in Fig. 16(d) show that the component in the flow direction ( $A_{33}$ ) is greater than other  $A_{22}$  and  $A_{11}$  components. In addition, due to the asymmetric velocity profile in Region 2, it can be observed that  $A_{33}$  values obtained through both modeling and experiments are slightly higher at  $y = 0$  mm compared to  $y = 4.5$  mm. Furthermore, the experimental orientation distribution appears only weakly dependent on the  $y$ -coordinate. This could suggest that the velocity distribution is more plug-flow-like and does not stabilize (or there is substantially more slip in the entrance region) by the time the fluid reaches Region 2.

## VI. CONCLUSIONS

A comprehensive procedure for the modeling of orientation distribution in wood fiber based composites has been successfully elaborated in this study. The procedure comprises (i) a numerical flow model of an

26 September 2024 06:35:40



extrusion die, coupled with generalized Newtonian constitutive equations and the Folger–Tucker formalism for accounting for the presence of the wood fiber; (ii) an experimental set of procedures based on capillary rheometry to provide or enable all the required material functions and boundary conditions required by the numerical model; (iii) and experimental protocol for the validation of melt pressure estimations with *in situ* data during extrusion and the estimation of die *in situ* fiber orientation. We especially highlight the importance of considering the slip conditions for adequate numerical results and for understanding the processing behavior of highly filled biocomposites. Within this procedural framework, the results showed a good agreement between the experimental and numerical orientation wood fiber distributions. Such results are significant building blocks for the design of processing elements streamlined to overcome challenges encountered when processing WPCs containing significant amounts of wood fiber content.

This study successfully integrated experimental and numerical methods. Future research could build on this by examining how input parameters influence the fiber pressure profile or orientation status. Several limitations and simplifications were present in this study, such as: (1) Assuming incompressibility, excluding the energy equation and heat dissipation, and using the SRF method instead of RSC or other approaches. (2) The accuracy of the model depends on various parameters, including the interaction coefficient (CI) and the aspect ratio of the fibers; determining these parameters can be challenging. (3) In the FT model, the fibers were assumed to be rigid and uniform; however, in practice, the nature of wood fibers is non-uniform and flexible. (4) SEM imaging and subsequent image analysis were used for experimental validation to model fiber orientation. Future studies might employ methods such as x-ray tomography for 3D fiber orientation to validate numerical simulation results more comprehensively. It is essential to recognize that this study is not exhaustive and contains certain research gaps. Thus, there is considerable potential and scope for future work in this area.

### SUPPLEMENTARY MATERIAL

See the [supplementary material](#), which provides slip length fitting parameters, images of the film die, a schematic illustration for flow rate measurements, mass and volumetric flow rates, inlet and outlet velocities, additional inlet pressure data not included in the main manuscript, and error measurements for pressures at the die inlet, along with other details.

### ACKNOWLEDGMENTS

This work has been carried out within the “Biocomposite” program generously funded by the Knut and Alice Wallenberg foundation (Dnr. KAW 2018.0451). S.P. and R.K. are grateful to acknowledge the financial support of Stora Enso Oyj to the program. R.K. and V.G. are grateful for the financial support of the “2D material-based technology for industrial applications” 2D-TECH Vinnova Competence Centre (Ref. 2019-00068). R.K. and V.G. are also grateful for the additional support of the Chalmers Area of Advance Materials Science, Chalmers Area of Advance Nano, and Chalmers Area of Advance Production.

### AUTHOR DECLARATIONS

#### Conflict of Interest

The authors have no conflicts to disclose.

### Author Contributions

**Sajjad Pashazadeh:** Conceptualization (lead); Data curation (lead); Formal analysis (lead); Investigation (lead); Methodology (lead); Project administration (equal); Software (lead); Validation (lead); Visualization (lead); Writing – original draft (lead); Writing – review & editing (lead). **Arvinth Seshadri Suresh:** Data curation (equal); Investigation (equal); Visualization (supporting); Writing – original draft (supporting). **Viney Ghai:** Data curation (supporting); Investigation (supporting); Methodology (supporting); Validation (supporting). **Tobias Moberg:** Conceptualization (supporting); Funding acquisition (equal); Investigation (supporting); Resources (lead); Supervision (equal); Writing – original draft (supporting). **Anders Brolin:** Conceptualization (supporting); Funding acquisition (lead); Investigation (supporting); Project administration (equal); Resources (supporting); Supervision (equal); Writing – original draft (supporting). **Roland Kadar:** Conceptualization (equal); Data curation (supporting); Formal analysis (supporting); Funding acquisition (lead); Investigation (supporting); Methodology (supporting); Project administration (lead); Resources (lead); Supervision (lead); Validation (supporting); Writing – original draft (equal); Writing – review & editing (supporting).

### DATA AVAILABILITY

The data that support the findings of this study are available from the corresponding authors upon reasonable request.

### REFERENCES

- <sup>1</sup>L. Sobczak, R. W. Lang, and A. Haider, “Polypropylene composites with natural fibers and wood—general mechanical property profiles,” *Compos. Sci. Technol.* **72**(5), 550–557 (2012).
- <sup>2</sup>S.-Y. Leu, T.-H. Yang, S.-F. Lo, and T.-H. Yang, “Optimized material composition to improve the physical and mechanical properties of extruded wood–plastic composites (WPCS),” *Constr. Build. Mater.* **29**, 120–127 (2012).
- <sup>3</sup>P. Nygård, B. Tanem, T. Karlsen, P. Brachet, and B. Leinsvang, “Extrusion-based wood fibre–PP composites: Wood powder and pelletized wood fibres—a comparative study,” *Compos. Sci. Technol.* **68**(15–16), 3418–3424 (2008).
- <sup>4</sup>A. Sudár, C. Burgstaller, K. Renner, J. Móczó, and B. Pukánszky, “Wood fiber reinforced multicomponent, multiphase PP composites: Structure, properties, failure mechanism,” *Compos. Sci. Technol.* **103**, 106–112 (2014).
- <sup>5</sup>Y. Guo, S. Zhu, Y. Chen, and D. Li, “Thermal properties of wood-plastic composites with different compositions,” *Materials* **12**(6), 881 (2019).
- <sup>6</sup>F. M. Coutinho, T. H. Costa, and D. L. Carvalho, “Polypropylene–wood fiber composites: Effect of treatment and mixing conditions on mechanical properties,” *J. Appl. Polym. Sci.* **65**(6), 1227–1235 (1997).
- <sup>7</sup>S. Pashazadeh, R. Ghanbari, M. Bek, A. Aulova, T. Moberg, A. Brolin, and R. Kádár, “Mapping surface defects in highly-filled wood fiber polymer composite extrusion from inline spectral analysis,” *Compos. Sci. Technol.* **242**, 110133 (2023).
- <sup>8</sup>V. Mazzanti and F. Mollica, “A review of wood polymer composites rheology and its implications for processing,” *Polymers* **12**(10), 2304 (2020).
- <sup>9</sup>H. Azizi and I. Ghasemi, “Investigation on the dynamic melt rheological properties of polypropylene/wood flour composites,” *Polym. Compos.* **30**(4), 429–435 (2009).
- <sup>10</sup>K. Pušnik Črešnar, L. Fras Zemljič, L. Slemenik Perše, and M. Bek, “Effect of wood fiber loading on the chemical and thermo-rheological properties of unrecycled and recycled wood-polymer composites,” *Appl. Sci.* **10**(24), 8863 (2020).
- <sup>11</sup>A. A. Klyosov, *Wood-Plastic Composites* (John Wiley & Sons, 2007).
- <sup>12</sup>M. Saddem, A. Koubaa, H. Bouafif, S. Migneault, and B. Riedl, “Effect of fiber and polymer variability on the rheological properties of wood polymer composites during processing,” *Polym. Compos.* **40**(S1), E609–E616 (2019).

- <sup>13</sup>K. Lewandowski, K. Piszczek, S. Zajchowski, and J. Mirowski, "Rheological properties of wood polymer composites at high shear rates," *Polym. Test.* **51**, 58–62 (2016).
- <sup>14</sup>V. Mazzanti, F. Mollica, and N. El Kissi, "Rheological and mechanical characterization of polypropylene-based wood plastic composites," *Polym. Compos.* **37**(12), 3460–3473 (2016).
- <sup>15</sup>R. Ou, Y. Xie, M. P. Wolcott, F. Yuan, and Q. Wang, "Effect of wood cell wall composition on the rheological properties of wood particle/high density polyethylene composites," *Compos. Sci. Technol.* **93**, 68–75 (2014).
- <sup>16</sup>K. Wilczyński, A. Nastaj, A. Lewandowski, K. J. Wilczyński, and K. Buziak, "Fundamentals of global modeling for polymer extrusion," *Polymers* **11**(12), 2106 (2019).
- <sup>17</sup>J. L. White and H. Potente, *Screw Extrusion* (Hanser Publishers Munich, Germany, 2001).
- <sup>18</sup>M. Hyvärinen, R. Jabeen, and T. Kärki, "The modelling of extrusion processes for polymers—A review," *Polymers* **12**(6), 1306 (2020).
- <sup>19</sup>J.-F. Agassant, P. Avenas, P. J. Carreau, B. Vergnes, and M. Vincent, *Polymer Processing: Principles and Modeling* (Carl Hanser Verlag GmbH Co. KG, 2017).
- <sup>20</sup>K. Wilczyński, K. Buziak, K. J. Wilczyński, A. Lewandowski, and A. Nastaj, "Computer modeling for single-screw extrusion of wood–plastic composites," *Polymers* **10**(3), 295 (2018).
- <sup>21</sup>K. Wilczyński, K. Buziak, A. Lewandowski, A. Nastaj, and K. J. Wilczyński, "Rheological basics for modeling of extrusion process of wood polymer composites," *Polymers* **13**(4), 622 (2021).
- <sup>22</sup>K. J. Wilczyński and K. Buziak, "Simulation of single screw extrusion of wood plastic composites based on the on-line pressure measurements," *Polimery* **64**(2), 135–142 (2019).
- <sup>23</sup>F. Liese and O. Wünsch, "Numerical simulation of flow processes of wood-polymer in extrusion dies," *Proc. Appl. Math. Mech.* **20**(1), e202000221 (2021).
- <sup>24</sup>N. Gonçalves, P. Teixeira, L. Ferrás, A. Afonso, J. Nóbrega, and O. Carneiro, "Design and optimization of an extrusion die for the production of wood–plastic composite profiles," *Polym. Eng. Sci.* **55**(8), 1849–1855 (2015).
- <sup>25</sup>T. Paphthasiou and A. Bénard, *Flow-Induced Alignment in Composite Materials* (Woodhead Publishing, 2021).
- <sup>26</sup>G. B. Jeffery, "The motion of ellipsoidal particles immersed in a viscous fluid," *Proc. R. Soc. London, Ser. A* **102**(715), 161–179 (1922).
- <sup>27</sup>F. Folgar and C. L. Tucker III, "Orientation behavior of fibers in concentrated suspensions," *J. Reinf. Plast. Compos.* **3**(2), 98–119 (1984).
- <sup>28</sup>E. Bagley, "End corrections in the capillary flow of polyethylene," *J. Appl. Phys.* **28**(5), 624–627 (1957).
- <sup>29</sup>B. Rabinowitsch, "Über die viskosität und elastizität von solen," *Z. Phys. Chem.* **145A**(1), 1–26 (1929).
- <sup>30</sup>M. Mooney, "Explicit formulas for slip and fluidity," *J. Rheol.* **2**(2), 210–222 (1931).
- <sup>31</sup>S. G. Hatzikiriakos, "Wall slip of molten polymers," *Prog. Polym. Sci.* **37**(4), 624–643 (2012).
- <sup>32</sup>F. Brochard and P. de Gennes, "Shear-dependent slippage at a polymer/solid interface," *Langmuir* **8**(12), 3033–3037 (1992).
- <sup>33</sup>M. Kroupa, M. Soos, and J. Kosek, "Slip on a particle surface as the possible origin of shear thinning in non-Brownian suspensions," *Phys. Chem. Chem. Phys.* **19**(8), 5979–5984 (2017).
- <sup>34</sup>R. Gallagher, *Finite Element Analysis—Fundamentals* (Prentice Hall, 1975).
- <sup>35</sup>M. M. Denn, *Polymer Melt Processing: Foundations in Fluid Mechanics and Heat Transfer* (Cambridge University Press, 2008).
- <sup>36</sup>S. Brown, "Boundary layer theory, 8th edn. by H. Schlichting & K. Gersten. Springer 2000. 799 pp. ISBN 3–540-66270–7. DM 179," *J. Fluid Mech.* **415**, 346–347 (2000).
- <sup>37</sup>C. G. Gogos and Z. Tadmor, *Principles of Polymer Processing* (John Wiley & Sons, 2013).
- <sup>38</sup>C. L. Tucker III, *Fundamentals of Fiber Orientation: Description, Measurement and Prediction* (Carl Hanser Verlag GmbH & Company KG, 2022).
- <sup>39</sup>S. M. Dinh and R. C. Armstrong, "A rheological equation of state for semiconcentrated fiber suspensions," *J. Rheol.* **28**(3), 207–227 (1984).
- <sup>40</sup>G. L. Hand, "A theory of anisotropic fluids," *J. Fluid Mech.* **13**(1), 33–46 (1962).
- <sup>41</sup>M. Doi, "Molecular dynamics and rheological properties of concentrated solutions of rodlike polymers in isotropic and liquid crystalline phases," *J. Polym. Sci., Polym. Phys. Ed.* **19**(2), 229–243 (1981).
- <sup>42</sup>S. G. Advani and C. L. Tucker III, "The use of tensors to describe and predict fiber orientation in short fiber composites," *J. Rheol.* **31**(8), 751–784 (1987).
- <sup>43</sup>S. G. Advani and C. L. Tucker III, "Closure approximations for three-dimensional structure tensors," *J. Rheol.* **34**(3), 367–386 (1990).
- <sup>44</sup>J. S. Cintra, Jr. and C. L. Tucker III, "Orthotropic closure approximations for flow-induced fiber orientation," *J. Rheol.* **39**(6), 1095–1122 (1995).
- <sup>45</sup>D. H. Chung and T. H. Kwon, "Invariant-based optimal fitting closure approximation for the numerical prediction of flow-induced fiber orientation," *J. Rheol.* **46**(1), 169–194 (2002).
- <sup>46</sup>M. Sepehr, G. Ausias, and P. J. Carreau, "Rheological properties of short fiber filled polypropylene in transient shear flow," *J. Non-Newtonian Fluid Mech.* **123**(1), 19–32 (2004).
- <sup>47</sup>H. M. Huynh, "Improved fiber orientation predictions for injection-molded composites," Ph.D. thesis (University of Illinois at Urbana-Champaign, 2001).
- <sup>48</sup>J. Wang, *Improved Fiber Orientation Predictions for Injection Molded Composites* (University of Illinois at Urbana-Champaign, 2007).
- <sup>49</sup>A. P. Eberle, D. G. Baird, P. Wapperom, and G. M. Vélaz-García, "Using transient shear rheology to determine material parameters in fiber suspension theory," *J. Rheol.* **53**(3), 685–705 (2009).
- <sup>50</sup>A. P. Eberle, G. M. Vélaz-García, D. G. Baird, and P. Wapperom, "Fiber orientation kinetics of a concentrated short glass fiber suspension in startup of simple shear flow," *J. Non-Newtonian Fluid Mech.* **165**(3–4), 110–119 (2010).
- <sup>51</sup>R. S. Bay, *Fiber Orientation in Injection-Molded Composites: A Comparison of Theory and Experiment* (University of Illinois at Urbana-Champaign, 1991).
- <sup>52</sup>C. Navier, "Mémoire sur les lois du mouvement des fluides," *Mém. Acad. R. Sci. Inst. France* **6**(1823), 389–440 (1823).
- <sup>53</sup>B. N. Sharma, D. Naragani, B. N. Nguyen, C. L. Tucker, and M. D. Sangid, "Uncertainty quantification of fiber orientation distribution measurements for long-fiber-reinforced thermoplastic composites," *J. Compos. Mater.* **52**(13), 1781–1797 (2018).
- <sup>54</sup>R. Kádár, I. F. Naue, and M. Wilhelm, "First normal stress difference and in-situ spectral dynamics in a high sensitivity extrusion die for capillary rheometry via the hole effect," *Polymer* **104**, 193–203 (2016).